Highly Active and Durable Ultrasmall Pd Nanocatalyst Encapsulated in Ultrathin Silica Layers by Selective Deposition for Formic Acid Oxidation

Jiefei Shan,[†,‡] Zhao Lei,[†,‡] Wei Wu,[†,‡] Yangyang Tan,[†,‡] Niancai Cheng,*[,†,‡] and Xueliang Sun*[,§]

[†]College of Materials Science and Engineering and [‡]Key Laboratory of Eco-materials Advanced Technology, Fuzhou University, Fuzhou 350108, China

[§]Department of Mechanical and Materials Engineering, The University of Western Ontario, London, Ontario N6A 5B9, Canada

S Supporting Information

ABSTRACT: The low performance of palladium (Pd) is a considerable challenge for direct formic acid fuel cells in practical applications. Herein, we develop a simple strategy to synthesize a highly active and durable Pd nanocatalyst encapsulated in ultrathin silica layers with vertically aligned nanochannels covered graphene oxides (Pd/rGO@pSiO$_2$) without blocking active sites by selective deposition. The Pd/rGO@pSiO$_2$ catalyst exhibits very high performance for a formic acid oxidation (FAO) reaction compared with the Pd/rGO without protective silica layers and commercial Pd/C catalysts. Pd/rGO@pSiO$_2$ shows an FAO activity 3.9 and 3.8 times better than those of Pd/rGO and Pd/C catalysts, respectively. The Pd/rGO@pSiO$_2$ catalysts are also almost 6-fold more stable than Pd/C and more than 3-fold more stable than Pd/rGO. The outstanding performance of our encapsulated Pd catalysts can be ascribed to the novel design of nanostructures by selective deposition fabricating ultrasmall Pd nanoparticles encapsulated in ultrathin silica layers with vertically aligned nanochannels, which not only avoid blocking the active sites but also facilitate the mass transfer in encapsulated catalysts. Our work indicates an important method to the rational design of high-performance catalysts for fuel cells in practical applications.

KEYWORDS: selective deposition, encapsulated nanoparticles, Pd catalysts, formic acid oxidation, ultrathin silica layers
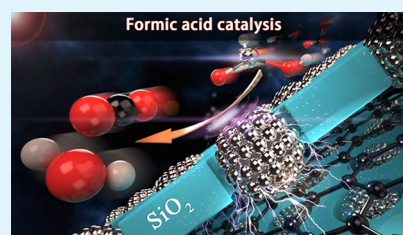
1. INTRODUCTION

Direct formic acid fuel cells (DFAFCs) are believed to be an ideal alternative energy source for electrical vehicles and portable electronic devices due to their high efficiency, high volumetric energy density, fewer fuel crossover issues, and easy storage of the liquid fuels.[1−6] Palladium (Pd) has been considered as the most efficient electrocatalyst material for electrochemical formic acid oxidation (FAO) because of its low oxidation overpotential and high CO tolerance.[7−12] To effectively utilize Pd, Pd nanoparticles (NPs) are generally supported on substrates including carbon and oxide materials to facilitate an FAO reaction. However, Pd NPs still suffer from insufficient long-term stability in the acidic electrochemical reaction conditions, resulting in the loss of Pd performance due to the dissolution of Pd NPs and Pd NP agglomeration caused by easy migration of the NPs on the supports.[13−17] The instability of Pd at the anode is a big challenge for the widespread commercial application of DFAFC technology. Another challenge for Pd catalysts is the synthesis of an ultrasmall Pd particle, ranging from subnanometer to about 2 nm, which will enhance Pd electrochemical activity and decrease the cost of DFAFCs.[15] Thus, it is extremely desirable to develop durable ultrasmall Pd catalysts with high activity toward FAO that can withstand the DFAFC harsh conditions and thus prevent performance loss resulting from Pd dissolution and NP migration and agglomeration on supports.

One of the efficient methods to achieve highly stable catalysts with high activity is encapsulating metal nanoparticles with electrochemically stable porous materials such as carbon, silica, cerium oxide, and zirconium, which can effectively suppress the sintering of metal NPs and alleviate leaching of dissolved metal NPs.[18−24] Among various stable materials, silica is an ideal encapsulating material due to one of the most abundant materials and its high thermal and excellent chemical stability in acidic medium.[19,25] It is reported that a good architecture of encapsulated metal NPs not only prevents sintering and agglomeration of the catalyst under long-term catalysis but also provides enough pore or channel for mass transfer.[26−28] The precise control of the thickness of porous layers is very important because very thin porous layers are not effectively protecting the metal NPs, while very thick ones lead to the loss of catalytic activity resulting from increasing mass transfer resistance and blocking the active sites.[29,30] In addition, tuning the pore size of porous layers is crucial for the high activity of encapsulated metal NPs because the porous layers also act as diffusion barriers.[31] The most reported encapsulation of metal nanoparticles were usually fabricated by the first synthesis of metal NPs or deposition of metal NPs on

Scheme 1. Strategy for the Synthesis of Small-Sized Pd Nanoparticles Selectively Grown Into the Pore Channel of rGO@pSiO$_2$
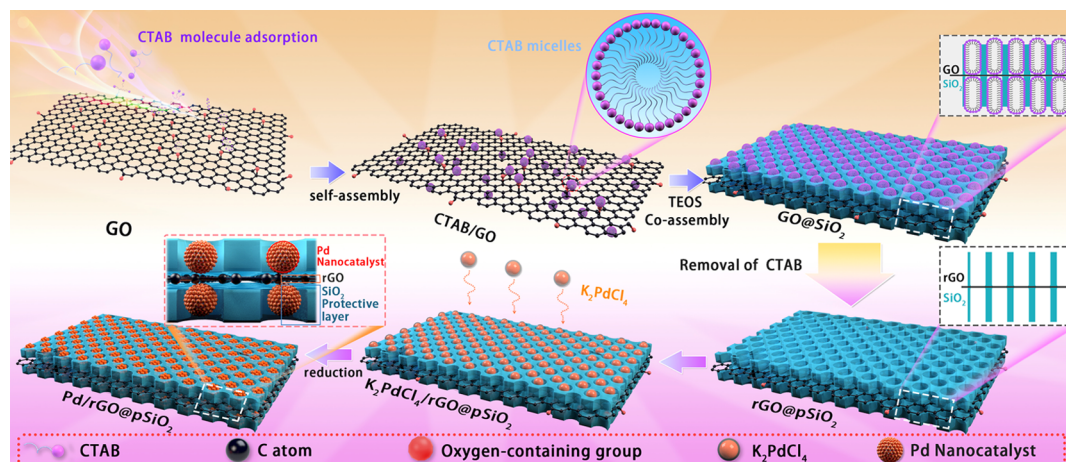
supports followed by covering porous layers and generating a pore through high-temperature treatment.[32−34] Although encapsulated metal NPs show enhanced stability, the protective layers can decrease the activity of metal NPs through blocking the active sites and increasing mass transfer resistance. So, it is very important to develop a new synthesis strategy to design highly stable encapsulated metal NPs, which not only avoid blocking the active sites but also facilitate the mass transfer in encapsulated catalysts.

Here, a facile approach is proposed to stabilize ultrasmall Pd NPs encapsulated in ultrathin silica layers with vertically aligned nanochannels without blocking the active sites by selective deposition. An outline of the synthetic strategy for the Pd encapsulated in ultrathin porous silica layers is schematically illustrated in Scheme 1. Cetyltrimethylammonium bromide (CTAB) admicelles as the pore-generating agent were adsorbed onto the graphene oxide (GO) surface followed by the formation of ultrathin silica layers through co-assembling CTAB with the silicate species.[35,36] After the removal of CTAB into the silica layer-covered GO, the vertically aligned nanochannels formed into silica layers, and the ultrasmall Pd nanoparticles selectively grow into the nanochannels generated by CTAB through the redox reaction between the functional groups on GO and PdCl$_4^{2-}$. The prepared Pd catalysts encapsulated in ultrathin silica layer-covered GO display ultimate stability with excellent catalytic FAO performance. The outstanding performance of our encapsulated catalysts is attributed to the fabrication of ultrasmall Pd NPs encapsulated into vertically aligned nanochannels of ultrathin silica layers by selective deposition.

2. EXPERIMENTAL SECTION

2.1. Synthesis of Pd/rGO@pSiO$_2$. We first prepared graphene oxide (GO) by a modified Hummers' method.[37] For the synthesis of the Pd/rGO@pSiO$_2$ catalysts, 2 g of CTAB and 80 mg of NaOH were first added into the dispersion solution containing 60 mg of GO and then ultrasonicated for 2 h. After magnetic stirring for 2 h at 40 °C, 0.1 mL of tetraethyl orthosilicate (TEOS) was added dropwise to the mixture. After stirring for another 10 min, the graphene oxide-covered silica layers (GO@pSiO$_2$) were washed several times with both water and ethanol and then freeze-dried. To remove the remaining CTAB, the as-prepared GO@pSiO$_2$ was further treated at 300 °C for 1 h in air followed by treatment at 300 °C under a N$_2$ atmosphere for 1 h. Then, 3 mL of K$_2$PdCl$_4$ (4 mg/mL) was added into 100 mL of water containing synthesized rGO@SiO$_2$ (30 mg) under stirring. After 12 h of stirring, the Pd/rGO@pSiO$_2$ was achieved by centrifugation,

washed with deionized water, and dried. The Pd/rGO@pSiO$_2$ was heated at 300 °C in a 10%H$_2$/90%N$_2$ atmosphere for 2 h. The Pd loading for Pd/rGO@pSiO$_2$ is 9 wt % by inductively coupled plasma mass spectrometry (ICP-MS).

2.2. Synthesis of Pd/rGO. Simply, 60 mg of GO was well dispersed in the water solution with stirring and sonication, and then to which, 9.0 mL of K$_2$PdCl$_4$ (4 mg/mL) was added and stirred also for 12 h, separated, and washed with pure water; the resulting catalyst was also collected by filtering, drying, and treatment for 2 h at 300 °C at the atmosphere of H$_2$. The Pd loading for Pd/rGO is 15 wt % by ICP-MS.

2.3. Synthesis of Pd/rGO@SiO$_2$. The Pd/rGO@SiO$_2$ was obtained through the growth of Pd on GO according to the procedure of the synthesis of Pd/rGO without the heating treatment. Then, the product was covered with silica layers followed by treatment at 300 °C under a N$_2$ and H$_2$ atmosphere for 2 h.

2.4. Materials Characterization. The morphology of the catalysts was performed using atomic force microscopy (AFM; Agilent 5500), X-ray powder diffraction (XRD; Rigaku ULTIMA III), and transmission electron microscopy (TEM; FEI TECNAL G2F2O). X-ray photoelectron spectroscopy (XPS) was performed on a Thermo VG Scientific ESCALAB 250 spectrometer. The MICROMERITICES 3Flex was applied to determine the nitrogen adsorption−desorption isotherms of samples. Inductively coupled plasma mass spectrometry (ICP-MS) was performed on an iCAP7000 (Thermo Fisher Scientific).

2.5. Electrochemical Testing. A standard three-electrode cell was applied to characterize electrochemical measurements using an Autolab electrochemistry station at room temperature. The working electrodes were achieved by deposition of a 10 μL uniform catalyst ink prepared by an ultrasonicating catalyst (4 mg) in 4 mL of isopropanol and 40 μL of Nafion (5 wt %). Platinum wire was used as a counter electrode, while Ag/AgCl (sat. KCl) was used as a reference electrode. Prior to CO stripping, the electrode potential was first held at −0.16 V when CO was bubbled through the 0.5 M H$_2$SO$_4$ solution. After 20 min, N$_2$ was then bubbled to remove the free CO in the electrolyte. Electrochemical impedance spectroscopy (EIS) was tested in 0.25 M HCOOH + 0.5 M H$_2$SO$_4$ and the frequency ranging from 10^{-2} to 10^5 Hz.

3. RESULTS AND DISCUSSION

The ultrathin silica layer-covered GO using CTAB as the pore-generating agent was achieved by the precise control of the ratio of GO, CTAB, and TEOS and reaction time (detailed in the Supporting Information). The ultrathin silica layer-covered GO with the vertically aligned nanochannels (rGO@pSiO$_2$) was achieved after the removal of CTAB, as shown in Figure S1.[35,36] The structural features of the ultrathin silica layer-
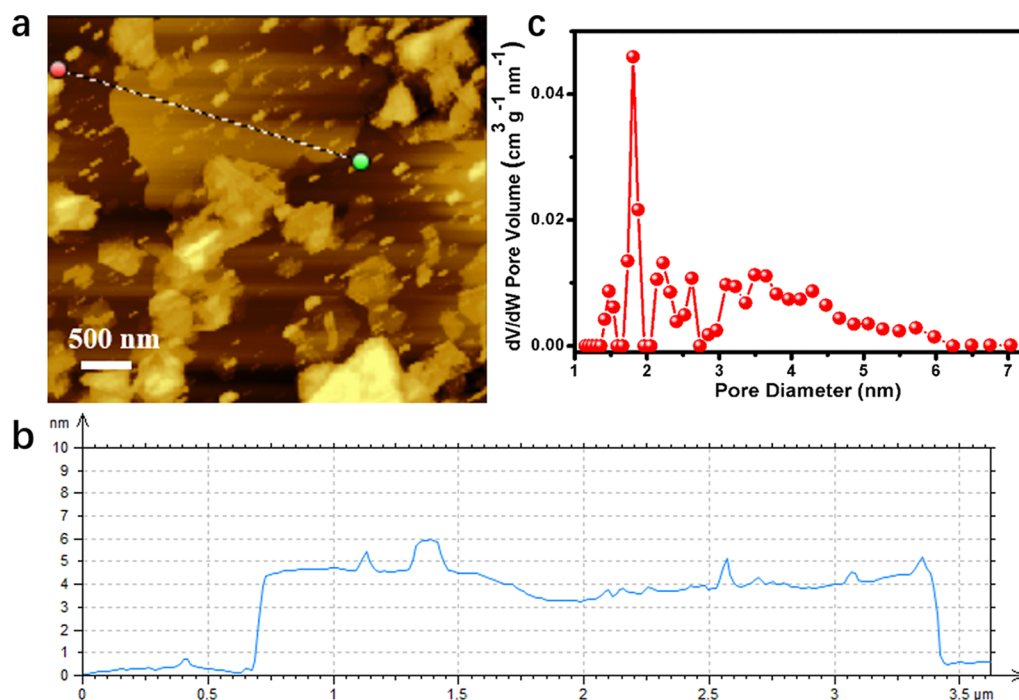
Figure 1. (a) AFM image and (b) corresponding thickness analysis from the line of the AFM image of the rGO@pSiO$_2$ sample. (c) Pore size distribution of the rGO@pSiO$_2$ sample.

covered GO were examined by atomic force microscopy (AFM) analyses. As shown in Figure 1a,b, the AFM image and thickness analyses reveal uniform ultrathin silica layer-covered GO, and the thickness of silica layers is approximately 2 nm. The pore size distributions of ultrathin silica layers in rGO@pSiO$_2$ were determined by N$_2$ adsorption−desorption (Figure 1c and Figure S2). It is observed that the rGO@pSiO$_2$ possesses narrow pore distribution for micropore centered at about 1.8 nm and broad mesopore size distribution centered at 3.5 nm in the range of about 2−6 nm (Figure 1c). As shown in Figure 2a,b, the uniform Pd NPs are highly dispersed into rGO@pSiO$_2$ and the average size of Pd NPs is 1.7 nm. The HRTEM image (Figure 2b) clearly indicates that the interplanar spacing is 0.23 nm, attributed to the (111) plane of face-centered cubic (fcc) Pd, which is consistent with the analysis of XRD data (Figure S3). In addition, the STEM elemental mapping (Figure 2c,d) reveals the uniform distribution of elemental carbon, silica, and Pd in Pd/rGO@pSiO$_2$. Figure S4 clearly demonstrates that the Pd nanocrystals without the use of silica layers are slightly agglomerated and have larger particle size (an average size of around 4.5 nm), which is similar to the results of a previous work.[38]

The above results clearly indicate that the silica layer-covered GO using CTAB as the pore-generating agent indeed facilitate the growth of ultrasmall Pd nanocrystals and uniform distribution on supports. The formation of ultrasmall Pd nanocrystals into rGO@pSiO$_2$ should be ascribed to the following factors: (i) The limited functional groups on GO. During the Pd growth into rGO@pSiO$_2$, the Pd precursor (PdCl$_4$$^{2-}$) first selectively reacts with the functional groups on the free surface of the graphene oxides generated by CTAB. The difference of the reduction potential of GO (0.48 V vs SCE) and PdCl$_4$$^{2-}$ (0.83 V vs SCE) is believed to be the driving force of Pd growth on GO,[38] where GO sheets act as the electron donors for reduction of Pd ions.[39] However, functional groups are limited on the substrate surface, which

restrain the growth of Pd NPs, leading to the ultrasmall Pd NPs in rGO@pSiO$_2$. (ii) Confined space of silica nano-channels. During Pd nucleation and particle growth, it is the natural tendency for metal atoms and NPs to prefer migration and aggregation to form larger particles, resulting in larger Pd NPs on GO without silica layers (Figure S4). Those nanochannels generated by CTAB into rGO@pSiO$_2$ provide a physical and energy barrier to inhibit the Pd NP migration on GO and thus effectively prevent sintering, leading to small-sized Pd NPs into rGO@pSiO$_2$ (Figure 2).

The metal valence states and surface composition of the Pd samples were studied by XPS. The full XPS spectrum clearly demonstrated the silica existence for rGO@pSiO$_2$ (Figure 3a and Figure S5). The fitting of the high-resolution Pd 3d spectrum (Figure 3b) shows four peaks for Pd/rGO@pSiO$_2$ whose peaks at 340.8 and 335.5 eV are assigned to the 3d$_{3/2}$ and 3d$_{5/2}$ of metallic Pd^0, respectively, and the peaks located at 342.1 and 336.9 eV are attributed to the 3d$_{3/2}$ and 3d$_{5/2}$ of Pd^{2+}, respectively.[40,41] It is clearly displayed that another binding energies approximately located at 339.0 and 344.0 eV are related to the 3d$_{5/2}$ and 3d$_{3/2}$ of Pd^{4+} for Pd/C and Pd/rGO, respectively.[42,43] Compared with Pd/C and Pd/rGO, the binding energies of Pd(0) and Pd(II) in Pd/rGO@pSiO$_2$ shift negatively. The negative shift of the Pd 3d binding energy favors the formic acid oxidation by lowering the intermediate chemisorption energy on the Pd surface.[44,45] Tables 1 and 2 summarize the binding energies of the Pd XPS signal and the mass percent of valence states in Pd/rGO@pSiO$_2$, Pd/rGO, and Pd/C catalysts. Table 2 indicates that the percentage of Pd(0) species of Pd/rGO@pSiO$_2$ is approximately 66.25% based on the curve fitting, higher than Pd/rGO (53.43%) and Pd/C (53.28%),which could promote the oxidation of formic acid due to high Pd(0) species as the origin of high activity.[46]

The electrochemical behaviors of as-prepared Pd samples were first evaluated by CV curves, as shown in Figure 4a. We calculate the electrochemical active surface areas (ECSAs) of
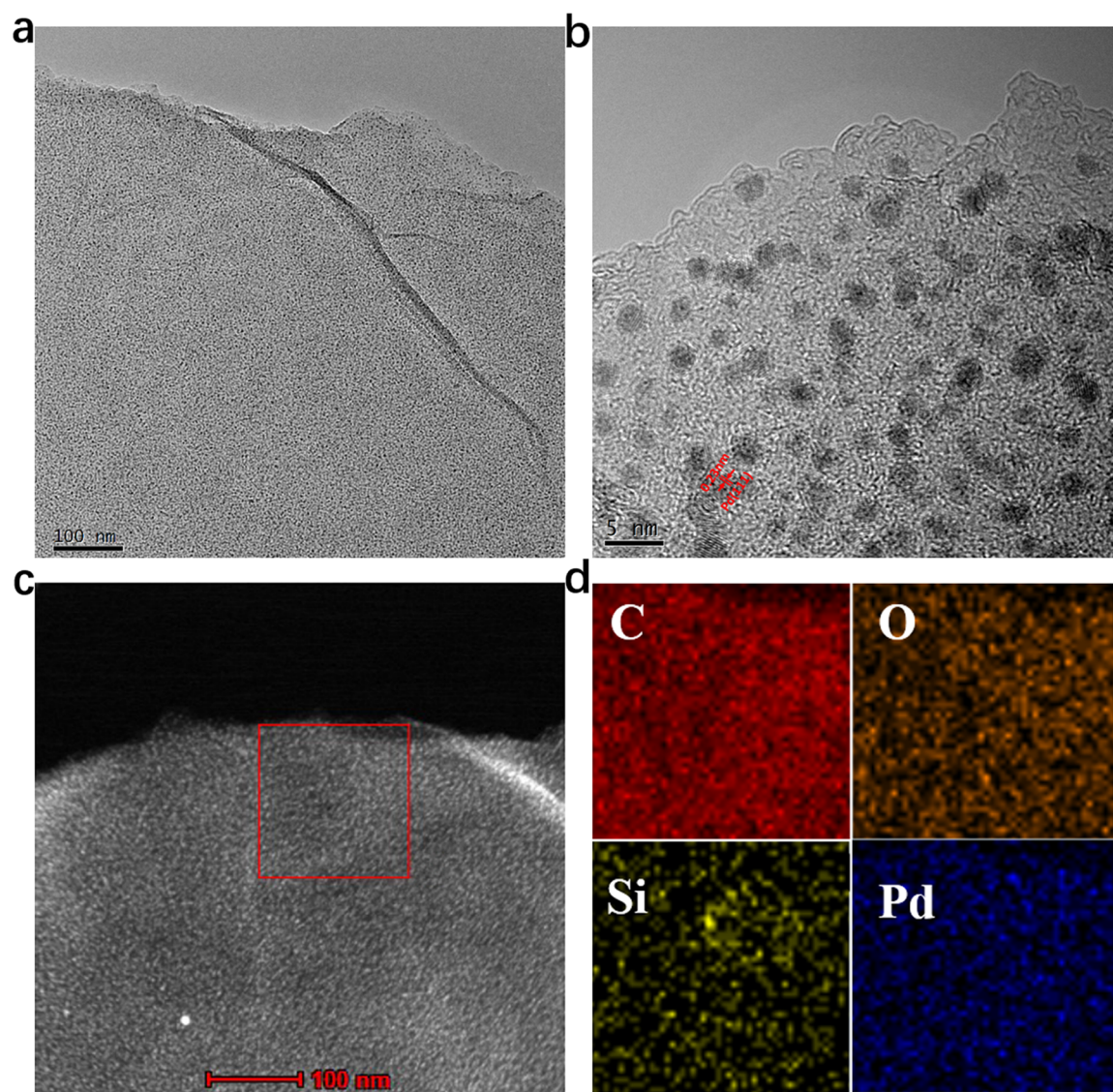
Figure 2. (a, b) TEM images of the Pd/rGO@pSiO$_2$ sample. (c) STEM image and (d) EDS mapping of the Pd/rGO@pSiO$_2$ sample.
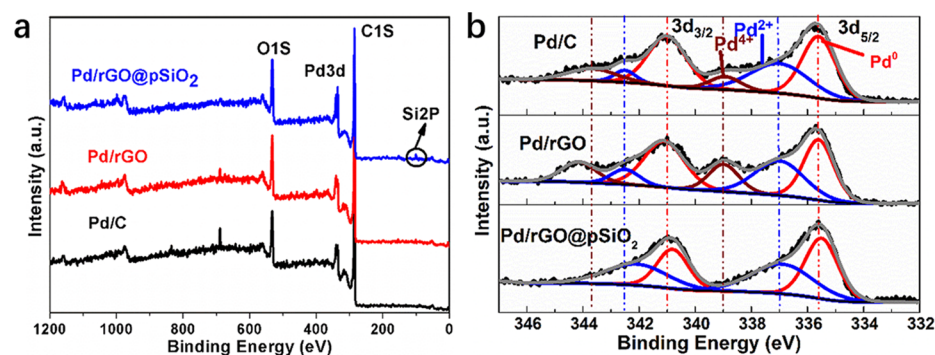

Figure 3. (a) XPS spectra and (b) high-resolution Pd 3d spectra of Pd/rGO@pSiO$_2$, Pd/rGO, and Pd/C samples.

Pd-based catalysts based on the electric charge of reduction of the Pd oxide monolayer.[47−49] The calculated ECSA of the Pd/rGO@pSiO$_2$ catalyst is 48.5 m^2 g$^{−1}$, larger than those of Pd/rGO (16.9 m^2 g$^{−1}$) and Pd/C (19.8 m^2 g$^{−1}$) catalysts. We measured the performance of the Pd/rGO@pSiO$_2$ catalyst toward FAO in comparison with benchmarks of Pd/rGO without silica layers and commercial Pd/C. The rGO@pSiO$_2$

without Pd did not show electrocatalytical activity toward FAO (Figure S6). Figure 4b shows the CV curves of Pd catalysts for FAO, in which the current is normalized to the loading amount of Pd catalysts on the electrode. It is found that the FAO on Pd/rGO@pSiO$_2$ starts at about −0.141 V, which negatively shifts by 42 and 14 mV (Figure 4b) in comparison with those of the Pd/C (−0.099 V) and Pd/rGO (−0.127 V) catalysts.

Table 1. Different Valence States of Pd Extracted from the Value of Binding Energy of Peaks in XPS Spectra for Pd/rGO@pSiO₂, Pt/rGO, and Pd/C Catalysts

XPS	Pd/C	Pd/rGO	Pd/rGO@pSiO₂
$Pd^0 3d_{5/2}$	335.6	335.6	335.5
$Pd^{2+} 3d_{5/2}$	337.0	337.0	336.9
$Pd^{4+} 3d_{5/2}$	339.0	339.0	
$Pd^0 3d_{3/2}$	341.0	341.1	340.8
$Pd^{2+} 3d_{3/2}$	342.5	342.5	342.1
$Pd^{4+} 3d_{3/2}$	343.66	344.15	

Table 2. Valence State Mass Percent of Pd^0, Pd^{2+}, and Pd^{4+} for Pd/rGO@pSiO₂, Pd/rGO, and Pd/C Catalysts, Respectively

XPS	Pd/C	Pd/rGO	Pd/rGO@pSiO₂
Pd^0	53.28	53.43	66.25
Pd^{2+}	34.45	23.4	33.75
Pd^{4+}	12.27	23.17	

The peak potential for FAO on the Pd/rGO@pSiO₂ catalyst is also observed to be more negative compared with the Pd/C catalyst, suggesting that the Pd/rGO@pSiO₂ catalyst more easily catalyzes FAO.[14] Moreover, the Pd/rGO@pSiO₂ catalyst indicates the highest forward peak current density (1.125 A mg⁻¹), which is about 3.9 and 3.8 times greater than those of the Pd/rGO (0.286 A mg⁻¹) and Pd/C catalysts (0.294 A mg⁻¹), respectively (Figure 4c). It is worth noting that the Pd/rGO@pSiO₂ catalyst shows the highest forward peak current density compared to the recently reported Pd-based FAO catalysts (Table S1). Those results imply that the Pd/rGO@pSiO₂ catalyst possesses superior catalytic activity toward FAO compared with Pd/rGO and Pd/C catalysts.

Impedance measurements (Figure 4d) were performed to further study the electrochemical behaviors of Pd/rGO@pSiO₂, Pd/C, and Pd/rGO toward FAO. It is believed that the diameter of the arc over the high−medium frequency region indicates the charge−transfer resistance (R_{ct}) of the FAO.[2,50] Compared with Pd/C and Pd/rGO catalysts, the Pd/rGO@pSiO₂ catalyst shows lower R_{ct}, suggesting that the vertically aligned nanochannels facilitate the mass transfer in encapsulated catalysts. As shown in Figure S7, the Pd/rGO@pSiO₂ possesses the most negative onset potentials for CO oxidation of 0.701 V, which is about 24 and 22 mV lower than those of Pd/C and Pd/rGO, respectively. In addition, the peak potential for CO oxidation at the Pd/rGO@pSiO₂ catalyst negatively shifts by about 40 mV compared with the Pd/rGO catalyst. These data indicate that the Pd/rGO@pSiO₂ catalyst has high CO tolerance.[51,52]

In addition to the outstanding performance of Pd/rGO@pSiO₂ in electrocatalyzing formic acid, Pd/rGO@pSiO₂ possesses high long-term stability during FAO, which is crucial for DFAFC practical applications. Compared with Pd/C and Pd/rGO catalysts, the polarization current of the Pd/rGO@pSiO₂ catalyst displays a much slower current decay during testing time (Figure 5a). After 6 h, the mass activity of the FAO on the Pd/rGO@pSiO₂ catalyst is 61.6 mA mg⁻¹ at 0.05 V. Remarkably, the mass activity of the Pd/rGO@pSiO₂ catalyst is about 128 and 693 times greater than the Pd/rGO catalyst (0.475 mA mg⁻¹) and Pd/C catalyst (0.104 mA mg⁻¹) after 6 h of stability test (Figure 5b). These findings suggest that the Pd/rGO@pSiO₂ catalyst possesses excellent electrochemical activity and stability toward FAO.

The accelerated durability tests (ADTs) were further applied to determine the electrochemical durability of the different Pd-based catalysts. The ADTs were performed by applying a
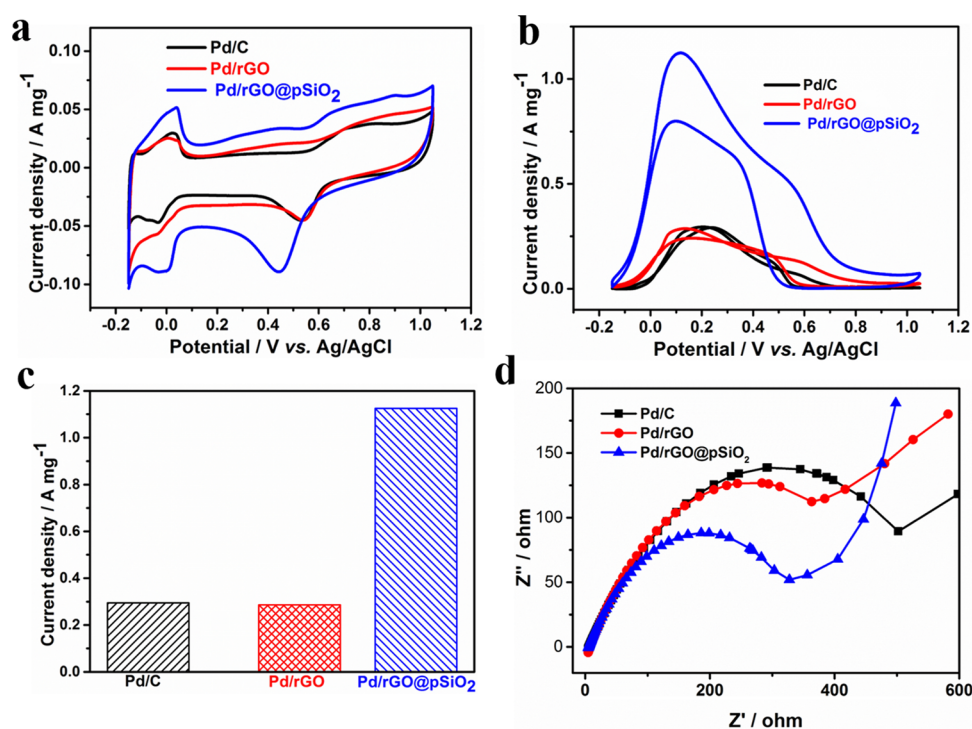
Figure 4. (a) CV curves of Pd/C, Pd/rGO, and Pd/rGO@pSiO₂ samples in the N₂-saturated 0.5 M H₂SO₄ solution. (b) CV curves and (c) the forward peak current density of Pd/C, Pd/rGO, and Pd/rGO@pSiO₂ samples in the N₂-saturated 0.25 M HCOOH + 0.5 M H₂SO₄ solution. (d) Nyquist plots of Pd/C, Pd/rGO, and Pd/rGO@pSiO₂ catalysts.
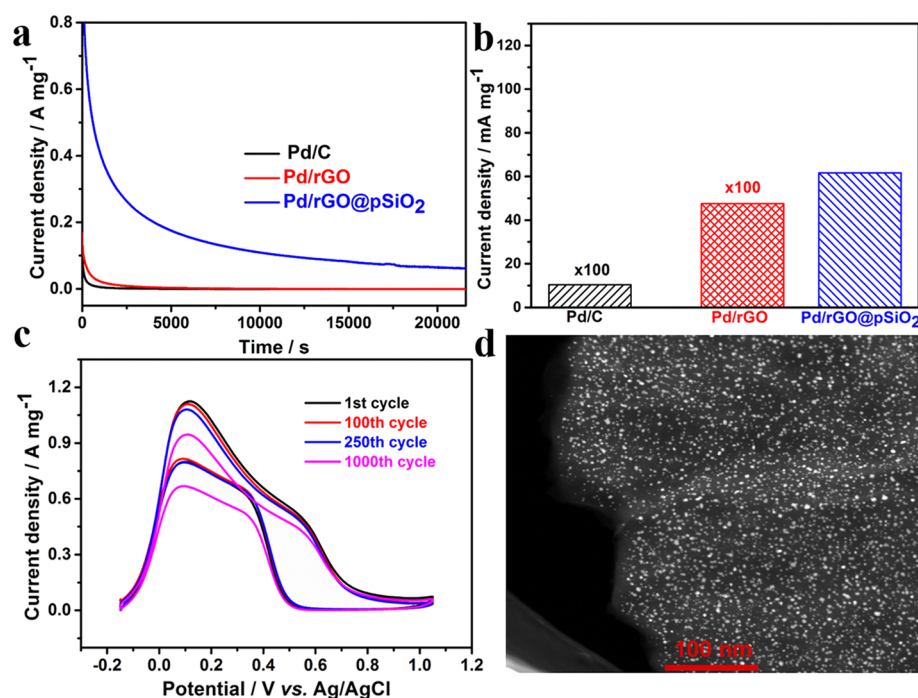
Figure 5. (a) CA curves at 0.05 V versus Ag/AgCl for 6 h and (b) the current density at 0.05 V versus Ag/AgCl at 6 h for different Pd-based catalysts in the N_2-saturated 0.25 M HCOOH + 0.5 M H_2SO_4 solution. (c) CV curves of electrodes made from Pd/rGO@pSiO$_2$ in the N_2-saturated 0.25 M HCOOH + 0.5 M H_2SO_4 solution during the durability tests. (d) STEM image of Pd/rGO@pSiO$_2$ after ADTs.

cycling potential between −0.15 and 1.05 V for 1000 cycles at a scan rate of 100 mV s^{-1} in the N_2-saturated 0.25 M formic acid + 0.5 M H_2SO_4 solution. The mass activity on Pd/rGO@pSiO$_2$ for FAO was only reduced by 1.6% after 100 cycles of CV measurements (Figure 5c), indicating its excellent FAOR stability. The mass activity of the Pd/rGO@pSiO$_2$ catalyst after 1000 cycles is still 0.945 A mg^{-1}, resulting in a loss of 16% only of its initial mass activity at the forward peak. The Pd/rGO@pSiO$_2$ catalyst also indicates higher stability in comparison with the most recently reported Pd catalysts as shown in Table S2. The STEM image analysis of Pd/rGO@pSiO$_2$ also indicates that there is no remarkable change in the Pd size of the catalyst after long-term cycling tests (Figures 5d and 2). By contrast, the catalytic activity of the Pd/C catalyst has been almost totally lost (95%) after 1000 cycles (Figure S8a). The Pd/rGO catalyst lost about 52% of initial peak current densities after 1000 cycles (Figure S8b). This finding demonstrates that the Pd/rGO@pSiO$_2$ catalyst is almost 6-fold more stable than Pd/C and more than 3-fold more stable than Pd/rGO (Figure S8c).

The CTAB as the pore-generating agent is crucial for determining the outstanding activity of Pd NPs in our encapsulation catalysts. The CTAB as the pore-generating agent generated the vertically aligned nanochannels for the Pd-selective deposition into the silica porous layer-covered GO, which not only facilitated the small-sized Pd formation but also avoided silica layers from blocking the active sites of the encapsulated metal nanoparticles. Figure S4 already indicates that the larger Pd NPs formed on the surface of graphene without silica nanochannel confinement. Then, the Pd NPs encapsulated in a porous silica layer (Pd/rGO@SiO$_2$) were achieved by the most reported method, which first prepared NPs followed by covering silica layers and generating a pore through high-temperature treatment.[33,53] As shown in Figure S9, the Pd/rGO@SiO$_2$ catalyst possesses micropore centered at 0.7 nm. Compared with Pd/rGO, the poor electrochemical FAO is achieved for Pd NPs in Pd/rGO@SiO$_2$ (Figure S10). The poor activity of Pd/rGO@SiO$_2$ may be contributed to some active sites of Pd NPs blocked by silica layers and the poor mass transfer for formic acid due to the small pore size of protective silica layers without using a pore-generating agent. Furthermore, the amount of CTAB also affects the activity of encapsulated Pd NPs toward FAO (Figure S11) because the silica layers with vertically aligned nanochannels were formed on the surface of GO at a narrow concentration range of CTAB.[35,36]

Based on the above discussion, the origins of the exceptional performance of Pd/rGO@pSiO$_2$ toward FAO could be attributed to the ultrasmall Pd NPs, pores generated in silica layers, and selective deposition. The small-sized nanochannels of silica layer-covered GO provide a physical and energy barrier to inhibit Pd NP migration on GO and thus effectively prevent sintering and then leading to small-sized Pd NPs, which enhance the activity of Pd catalysts. The pores generated in silica layers can favor the mass transfer of formic acid and expose more Pd-active sites, resulting in enhancing electrochemical formic acid oxidation activity. The selective deposition effectively avoids the protective layers (porous silica layers) that block some active sites on encapsulated metal NPs, resulting in high activity of Pd catalysts. Compared with Pd/C and Pd/rGO catalysts, the increased stability of Pd/rGO@pSiO$_2$ should be attributed to the sintering resistance of ultrathin porous silica layers designed by our new catalyst preparation strategy. Pd NPs encapsulated in porous silica layers could suppress detachment and agglomeration of Pd on support during a catalytic reaction.

4. CONCLUSIONS

We demonstrated a facile selective deposition approach to stabilize Pd catalysts encapsulated in ultrathin silica layers with

vertically aligned nanochannels. The Pd NPs encapsulated in the ultrathin silica layers indicate not only excellent activity but also extremely high stability toward electrochemical FAO. The Pd catalysts encapsulated in the ultrathin silica layers by selective deposition exhibit a low oxidation potential for FAO in comparison with Pd/C and Pd/rGO catalysts. More importantly, our Pd catalysts are also almost 6-fold more stable than Pd/C and more than 3-fold more stable than Pd/rGO. The remarkable performance of this novel catalyst is ascribed to the ultrasmall Pd NPs encapsulated in ultrathin silica layers with vertically aligned nanochannels by the selective deposition, which not only avoid blocking the active sites but also facilitate the mass transfer in encapsulated catalysts. The general synthetic approach presented here provides a promising strategy for designing high-performance metal catalysts.

■ ASSOCIATED CONTENT

ⓢ Supporting Information

The Supporting Information is available free of charge on the ACS Publications website at DOI: 10.1021/acsami.9b13451.

> Nitrogen adsorption−desorption isotherm of the rGo@ pSiO$_2$, XRD patterns of Pd/C, Pd/rGO, and Pd/rGO@ pSiO$_2$, TEM images of the Pd/rGO sample, XPS spectrum of the Si element in Pd/rGO@ pSiO$_2$, ADTs from Pd/C and Pd/rGO for FAO, N$_2$ adsorption−desorption isotherms, and pore size distribution and its formic acid oxidation performance of Pd/rGO@SiO$_2$ in this study (PDF)

■ AUTHOR INFORMATION

Corresponding Authors
*E-mail: niancaicheng@fzu.edu.cn (N.C.).
*E-mail: xsun@eng.uwo.ca (X.S.).

ORCID ⓘ
Niancai Cheng: 0000-0002-6358-5515
Xueliang Sun: 0000-0003-0374-1245

Notes
The authors declare no competing financial interest.

■ REFERENCES

(1) Zhang, L. Y.; Zhao, Z. L.; Li, C. M. Formic Acid-Reduced Ultrasmall Pd Nanocrystals on Graphene to Provide Superior Electocatalytic Activity and Stability toward Formic Acid Oxidation. *Nano Energy* **2015**, *11*, 71−77.

(2) Song, F.-Z.; Zhu, Q.-L.; Yang, X.; Zhan, W.-W.; Pachfule, P.; Tsumori, N.; Xu, Q. Metal-Organic Framework Templated Porous Carbon-Metal Oxide/Reduced Graphene Oxide as Superior Support of Bimetallic Nanoparticles for Efficient Hydrogen Generation from Formic Acid. *Adv. Energy Mater.* **2018**, *8*, 1701416.

(3) Wang, R.; Wang, C.; Cai, W. B.; Ding, Y. Ultralow-Platinum-Loading High-Performance Nanoporous Electrocatalysts with Nano-engineered Surface Structures. *Adv. Mater.* **2010**, *22*, 1845−1848.

(4) Chen, D.; Sun, P.; Liu, H.; Yang, J. Bimetallic Cu−Pd Alloy Multipods and Their Highly Electrocatalytic Performance for Formic Acid Oxidation and Oxygen Reduction. *J. Mater. Chem. A* **2017**, *5*, 4421−4429.

(5) Lee, S.-Y.; Jung, N.; Cho, J.; Park, H.-Y.; Ryu, J.; Jang, I.; Kim, H.-J.; Cho, E.; Park, Y.-H.; Ham, H. C.; Jang, J. H.; Yoo, S. J. Surface-Rearranged Pd3Au/C Nanocatalysts by Using CO-Induced Segrega-tion for Formic Acid Oxidation Reactions. *ACS Catal.* **2014**, *4*, 2402−2408.

(6) Du, C.; Chen, M.; Wang, W.; Yin, G. Nanoporous PdNi Alloy Nanowires As Highly Active Catalysts for the Electro-Oxidation of Formic Acid. *ACS Appl. Mater. Interfaces* **2011**, *3*, 105−109.

(7) Lou, M.; Wang, R.; Zhang, J.; Tang, X.; Wang, L.; Guo, Y.; Jia, D.; Shi, H.; Yang, L.; Wang, X.; Sun, Z.; Wang, T.; Huang, Y. Optimized Synthesis of Nitrogen and Phosphorus Dual-Doped Coal-Based Carbon Fiber Supported Pd Catalyst with Enhanced Activities for Formic Acid Electrooxidation. *ACS Appl. Mater. Interfaces* **2019**, *11*, 6431−6441.

(8) Mazumder, V.; Chi, M.; Mankin, M. N.; Liu, Y.; Metin, Ö.; Sun, D.; More, K. L.; Sun, S. A Facile Synthesis of MPd (M = Co, Cu) Nanoparticles and Their Catalysis for Formic Acid Oxidation. *Nano Lett.* **2012**, *12*, 1102−1106.

(9) Tian, N.; Lu, B.-A.; Yang, X.-D.; Huang, R.; Jiang, Y.-X.; Zhou, Z.-Y.; Sun, S.-G. Rational Design and Synthesis of Low-Temperature Fuel Cell Electrocatalysts. *Electrochem. Energy Rev.* **2018**, *1*, 54−83.

(10) Yang, N.; Zhang, Z.; Chen, B.; Huang, Y.; Chen, J.; Lai, Z.; Chen, Y.; Sindoro, M.; Wang, A. L.; Cheng, H.; Fan, Z.; Liu, X.; Li, B.; Zong, Y.; Gu, L.; Zhang, H. Synthesis of Ultrathin PdCu Alloy Nanosheets Used as a Highly Efficient Electrocatalyst for Formic Acid Oxidation. *Adv. Mater.* **2017**, *29*, 1700769.

(11) Yang, Y.; Xu, H.; Cao, D.; Zeng, X. C.; Cheng, D. Hydrogen Production via Efficient Formic Acid Decomposition: Engineering the Surface Structure of Pd-Based Alloy Catalysts by Design. *ACS Catal.* **2018**, *9*, 781−790.

(12) Maiyalagan, T.; Nassr, A. B. A.; Alaje, T. O.; Bron, M.; Scott, K. Three-dimensional Cubic Ordered Mesoporous Carbon (CMK-8) as Highly Efficient Stable Pd Electro-Catalyst Support for Formic Acid Oxidation. *J. Power Sources* **2012**, *211*, 147−153.

(13) Jiang, K.; Zhang, H.-X.; Zou, S.; Cai, W.-B. Electrocatalysis of Formic Acid on Palladium and Platinum Surfaces: from Fundamental Mechanisms to Fuel Cell Applications. *Phys. Chem. Chem. Phys.* **2014**, *16*, 20360−20376.

(14) Liu, Z.; Fu, G.; Li, J.; Liu, Z.; Xu, L.; Sun, D.; Tang, Y. Facile Synthesis Based on Novel Carbon-Supported Cyanogel of Structurally Ordered Pd3Fe/C as Electrocatalyst for Formic Acid Oxidation. *Nano Res.* **2018**, *11*, 4686−4696.

(15) Wang, X.; Yang, J.; Yin, H.; Song, R.; Tang, Z. "Raisin Bun"-Like Nanocomposites of Palladium Clusters and Porphyrin for Superior Formic Acid Oxidation. *Adv. Mater.* **2013**, *25*, 2728−2732.

(16) Zhang, L.; Wan, L.; Ma, Y.; Chen, Y.; Zhou, Y.; Tang, Y.; Lu, T. Crystalline Palladium−Cobalt Alloy Nanoassemblies with Enhanced Activity and Stability for The Formic Acid Oxidation Reaction. *Appl. Catal., B* **2013**, *138-139*, 229−235.

(17) Ren, M.; Kang, Y.; He, W.; Zou, Z.; Xue, X.; Akins, D. L.; Yang, H.; Feng, S. Origin of Performance Degradation of Palladium-Based Direct Formic Acid Fuel Cells. *Appl. Catal., B* **2011**, *104*, 49−53.

(18) Lu, P.; Campbell, C. T.; Xia, Y. A Sinter-Resistant Catalytic System Fabricated by Maneuvering The Selectivity of SiO$_2$ Deposition onto The TiO$_2$ Surface versus The Pt Nanoparticle Surface. *Nano Lett.* **2013**, *13*, 4957−4962.

(19) Joo, S. H.; Park, J. Y.; Tsung, C.-K.; Yamada, Y.; Yang, P.; Somorjai, G. A. Thermally Stable Pt/Mesoporous Silica Core-Shell Nanocatalysts for High-Temperature Reactions. *Nat. Mater.* **2009**, *8*, 126−131.

(20) Lu, J.; Fu, B.; Kung, M. C.; Xiao, G.; Elam, J. W.; Kung, H. H.; Stair, P. C. Coking- and Sintering-Resistant Palladium Catalysts

Achieved Through Atomic Layer Deposition. *Science* **2012**, *335*, 1205−1208.

(21) Cheng, K.; Kou, Z.; Zhang, J.; Jiang, M.; Wu, H.; Hu, L.; Yang, X.; Pan, M.; Mu, S. Ultrathin Carbon Layer Stabilized Metal Catalysts towards Oxygen Reduction. *J. Mater. Chem. A* **2015**, *3*, 14007−14014.

(22) Cho, H. J.; Kim, D.; Li, J.; Su, D.; Xu, B. Zeolite-Encapsulated Pt Nanoparticles for Tandem Catalysis. *J. Am. Chem. Soc.* **2018**, *140*, 13514−13520.

(23) Wan, C.; Cheng, D.-g.; Chen, F.; Zhan, X. Fabrication of CeO2 Nanotube Supported Pt Catalyst Encapsulated with Silica for High and Stable Performance. *Chem Commun* **2015**, *51*, 9785−9788.

(24) Song, S.; Wang, X.; Zhang, H. CeO$_2$-Encapsulated Noble Metal Nanocatalysts: Enhanced Activity and Stability for Catalytic Application. *NPG Asia Mater.* **2015**, *7*, No. e179.

(25) Robinson, J. E.; Labrador, N. Y.; Chen, H.; Sartor, B. E.; Esposito, D. V. Silicon Oxide-Encapsulated Platinum Thin Films as Highly Active Electrocatalysts for Carbon Monoxide and Methanol Oxidation. *ACS Catal.* **2018**, 11423−11434.

(26) Ji, X.; Lee, K. T.; Holden, R.; Zhang, L.; Zhang, J.; Botton, G. A.; Couillard, M.; Nazar, L. F. Nanocrystalline Intermetallics on Mesoporous Carbon for Direct Formic Acid Fuel Cell Anodes. *Nat. Chem.* **2010**, *2*, 286−293.

(27) Kim, H.; Robertson, A. W.; Kim, S. O.; Kim, J. M.; Warner, J. H. Resilient High Catalytic Performance of Platinum Nanocatalysts with Porous Graphene Envelope. *ACS Nano* **2015**, *9*, 5947−5957.

(28) Dumitrescu, I.; Crooks, R. M. Effect of Mass Transfer on The Oxygen Reduction Reaction Catalyzed by Platinum Dendrimer Encapsulated Nanoparticles. *Proc. Natl. Acad. Sci.* **2012**, *109*, 11493−11497.

(29) Tong, X.; Zhang, J.; Zhang, G.; Wei, Q.; Chenitz, R.; Claverie, J. P.; Sun, S. Ultrathin Carbon-Coated Pt/Carbon Nanotubes: A Highly Durable Electrocatalyst for Oxygen Reduction. *Chem. Mater.* **2017**, *29*, 9579−9587.

(30) Gao, Z.; Qin, Y. Design and Properties of Confined Nanocatalysts by Atomic Layer Deposition. *Acc. Chem. Res.* **2017**, *50*, 2309−2316.

(31) Takenaka, S.; Miyazaki, T.; Matsune, H.; Kishida, M. Highly Active and Durable Silica-Coated Pt Cathode Catalysts for Polymer Electrolyte Fuel cells: Control of Micropore Structures in Silica Layers. *Catal. Sci. Technol.* **2015**, *5*, 1133−1142.

(32) Lu, G.; Li, S.; Guo, Z.; Farha, O. K.; Hauser, B. G.; Qi, X.; Wang, Y.; Wang, X.; Han, S.; Liu, X.; DuChene, J. S.; Zhang, H.; Zhang, Q.; Chen, X.; Ma, J.; Loo, S. C. J.; Wei, W. D.; Yang, Y.; Hupp, J. T.; Huo, F. Imparting Functionality to A Metal−Organic Framework Material by Controlled Nanoparticle Encapsulation. *Nat. Chem.* **2012**, *4*, 310−316.

(33) Takenaka, S.; Miyamoto, H.; Utsunomiya, Y.; Matsune, H.; Kishida, M. Catalytic Activity of Highly Durable Pt/CNT Catalysts Covered with Hydrophobic Silica Layers for the Oxygen Reduction Reaction in PEFCs. *J. Phys. Chem. C* **2014**, *118*, 774−783.

(34) Haynes, T.; Ersen, O.; Dubois, V.; Desmecht, D.; Nakagawa, K.; Hermans, S. Protecting A Pd/CB Catalyst by A Mesoporous Silica Layer. *Appl. Catal., B* **2019**, *241*, 196−204.

(35) Wang, Z.-M.; Wang, W.; Coombs, N.; Soheilnia, N.; Ozin, G. A. Graphene Oxide−Periodic Mesoporous Silica Sandwich Nano-composites with Vertically Oriented Channels. *ACS Nano* **2010**, *4*, 7437−7450.

(36) Wang, Z.-M.; Peng, W.; Takenaka, Y.; Yoshizawa, N.; Kosuge, K.; Wang, W.; Ozin, G. A. Sandwich-Type Nanocomposite of Reduced Graphene Oxide and Periodic Mesoporous Silica with Vertically Aligned Mesochannels of Tunable Pore Depth and Size. *Adv. Funct. Mater.* **2017**, *27*, 1704066.

(37) Cheng, N.; Liu, J.; Banis, M. N.; Geng, D.; Li, R.; Ye, S.; Knights, S.; Sun, X. High Stability and Activity of Pt Electrocatalyst on Atomic Layer Deposited Metal Oxide/Nitrogen-Doped Graphene Hybrid Support. *Int. J. Hydrogen Energy* **2014**, *39*, 15967−15974.

(38) Chen, X.; Wu, G.; Chen, J.; Chen, X.; Xie, Z.; Wang, X. Synthesis of "Clean" and Well-Dispersive Pd Nanoparticles with Excellent Electrocatalytic Property on Graphene Oxide. *J. Am. Chem. Soc.* **2011**, *133*, 3693−3695.

(39) Yin, H.; Tang, H.; Wang, D.; Gao, Y.; Tang, Z. Facile Synthesis of Surfactant-Free Au Cluster/Graphene Hybrids for High-Performance Oxygen Reduction Reaction. *ACS Nano* **2012**, *6*, 8288−8297.

(40) Li, J.; Tian, Q.; Jiang, S.; Zhang, Y.; Wu, Y. Electrocatalytic Performances of Phosphorus Doped Carbon Supported Pd Towards Formic Acid Oxidation. *Electrochim. Acta* **2016**, *213*, 21−30.

(41) Ray, C.; Dutta, S.; Sahoo, R.; Roy, A.; Negishi, Y.; Pal, T. Fabrication of Nitrogen-Doped Mesoporous-Carbon-Coated Palladium Nanoparticles: An Intriguing Electrocatalyst for Methanol and Formic Acid Oxidation. *Chem. − Asian J.* **2016**, *11*, 1588−1596.

(42) Koo, W.-T.; Choi, S.-J.; Jang, J.-S.; Kim, I.-D. Metal-Organic Framework Templated Synthesis of Ultrasmall Catalyst Loaded ZnO/ZnCo$_2$O$_4$ Hollow Spheres for Enhanced Gas Sensing Properties. *Sci. Rep.* **2017**, *7*, 45074.

(43) Yamamoto, Y.; Matsuzaki, T.; Tanaka, S.; Nishihira, K.; Ohdan, K.; Nakamura, A.; Okamoto, Y. Catalysis and Characterization of Pd/NaY for Dimethyl Carbonate Synthesis From Methyl Nitrite and CO. *J. Chem. Soc., Faraday Trans.* **1997**, *93*, 3721−3727.

(44) Zhang, Z.; Ge, J.; Ma, L.; Liao, J.; Lu, T.; Xing, W. Highly Active Carbon-Supported PdSn Catalysts for Formic Acid Electro-oxidation. *Fuel Cells* **2009**, *9*, 114−120.

(45) Zhou, W. P.; Lewera, A.; Larsen, R.; Masel, R. I.; Bagus, P. S.; Wieckowski, A. Size Effects in Electronic and Catalytic Properties of Unsupported Palladium Nanoparticles in Electrooxidation of Formic Acid. *J. Phys. Chem. B* **2006**, *110*, 13393−13398.

(46) Liang, X.; Liu, B.; Zhang, J.; Lu, S.; Zhuang, Z. Ternary Pd-Ni-P Hybrid Electrocatalysts Derived from Pd-Ni Core-Shell Nano-particles with Enhanced Formic Acid Oxidation Activity. *Chem. Commun.* **2016**, *52*, 11143−11146.

(47) Koh, K.; Jeon, M.; Chevrier, D. M.; Zhang, P.; Yoon, C. W.; Asefa, T. Novel nanoporous N-Doped Carbon-Supported Ultrasmall Pd Nanoparticles: Efficient Catalysts for Hydrogen Storage and Release. *Appl. Catal., B* **2017**, *203*, 820−828.

(48) Ding, J.; Liu, Z.; Liu, X.; Liu, J.; Deng, Y.; Han, X.; Zhong, C.; Hu, W. Mesoporous Decoration of Freestanding Palladium Nanotube Arrays Boosts the Electrocatalysis Capabilities toward Formic Acid and Formate Oxidation. *Adv. Energy Mater.* **2019**, 1900955.

(49) Chowdhury, S. R.; Maiyalagan, T. Enhanced Electro-catalytic Activity of Nitrogen-doped Reduced Graphene Oxide Supported PdCu Nanoparticles for Formic Acid Electro-oxidation. *Int. J. Hydrogen Energy* **2019**, *44*, 14808−14819.

(50) Zhang, L. Y.; Zhao, Z. L.; Yuan, W.; Li, C. M. Facile One-Pot Surfactant-Free Synthesis of Uniform Pd6Co Nanocrystals on 3D Graphene as An Efficient Electrocatalyst toward Formic Acid Oxidation. *Nanoscale* **2016**, *8*, 1905−1909.

(51) Qiu, X.; Zhang, H.; Wu, P.; Zhang, F.; Wei, S.; Sun, D.; Xu, L.; Tang, Y. One-Pot Synthesis of Freestanding Porous Palladium Nanosheets as Highly Efficient Electrocatalysts for Formic Acid Oxidation. *Adv. Funct. Mater.* **2017**, *27*, 1603852.

(52) Xi, Z.; Erdosy, D. P.; Mendoza-Garcia, A.; Duchesne, P. N.; Li, J.; Muzzio, M.; Li, Q.; Zhang, P.; Sun, S. Pd Nanoparticles Coupled to WO$_{2.72}$ Nanorods for Enhanced Electrochemical Oxidation of Formic Acid. *Nano Lett.* **2017**, *17*, 2727−2731.

(53) Dai, Y.; Lim, B.; Yang, Y.; Cobley, C. M.; Li, W.; Cho, E. C.; Grayson, B.; Fanson, P. T.; Campbell, C. T.; Sun, Y.; Xia, Y. A Sinter-Resistant Catalytic System Based on Platinum Nanoparticles Supported on TiO$_2$ Nanofibers and Covered by Porous Silica. *Angew. Chem., Int. Ed.* **2010**, *49*, 8165−8168.